

Investigating the Oxygenation of Brain Arteriovenous Malformations Using Quantitative Susceptibility Mapping

Supplementary Material

Pre-GKR Patient	(a) Nidus Volume [ml]	(b) Hematocrit
AVM01	3.03	0.44
AVM02	8.73	n/a
AVM03	4.96	0.42
AVM04	0.56	0.40
AVM05	3.69	0.36
AVM06	5.87	n/a
AVM07	10.77	0.46
AVM08	1.32	0.44
AVM09	0.10	0.38
AVM10	2.10	0.42
AVM11	0.23	0.42
AVM12	1.29	0.46
AVM13	4.20	0.37
AVM14	7.63	0.93
AVM15	n/a	0.40
Mean \pm SD	3.89 \pm 3.35	0.41 \pm 0.03

Table S1 Nidus size and hematocrit values for each pre-GKR patient. The size of the nidus (**a**) was calculated based on DSA images acquired for GKR planning. The hematocrit (**b**) was measured within three weeks before the MRI experiment. Nidus size measurements were not available for one patient (AVM15), who decided not to undergo GKR after the MRI acquisition. Hematocrit measurements were not available for two patients (AVM02 and AVM06). The bottom row shows the mean and SD values of the nidus volume and hematocrit across patients, excluding the n/a values.

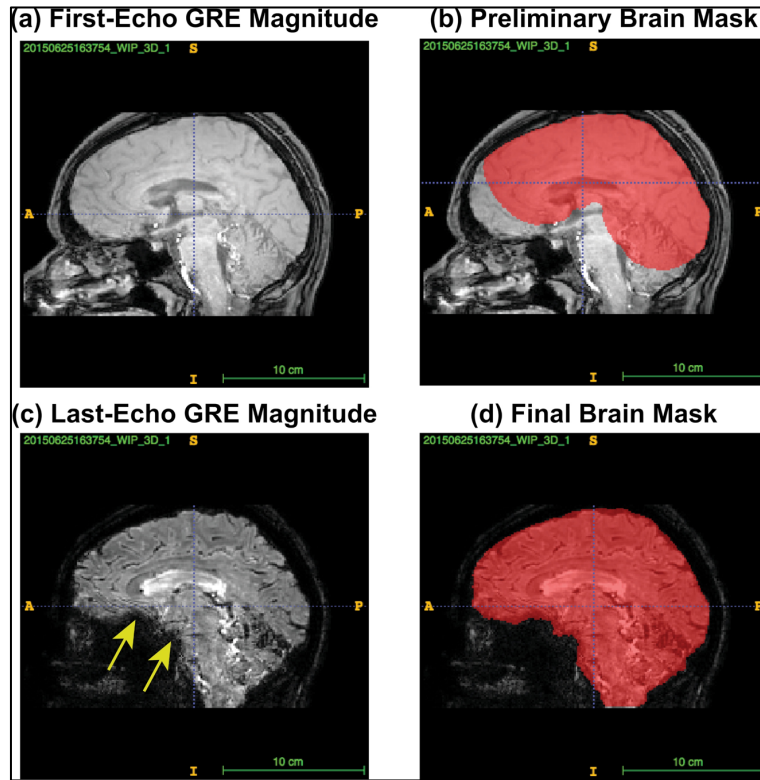


Fig. S1 ITK-SNAP-based brain masking. The first-echo GRE magnitude image **(a)** was used to calculate a preliminary brain mask (red overlay in **(b)**) including the SSS. The last-echo GRE magnitude image **(c)** was then used to mask the rest of the brain volume while excluding regions of signal dropout due to the presence of air-tissue interfaces (yellow arrows). The final brain mask is shown in **(d)**.

S1. Supplementary Methods

S1.1 Brain Mask Calculation

For both the 2D and 3D gradient-recalled echo (GRE) data sets, the brain mask for quantitative susceptibility mapping (QSM) was calculated based on the first-echo and seventh-echo magnitude images. The superior sagittal sinus (SSS) was fully visible only at shorter echo times (TEs). Therefore, the first-echo magnitude image (Fig. S1a) was used to create a preliminary brain mask that included the whole SSS. At this stage, the foreground was identified as the part of the magnitude image with intensities greater than 500,000 (3D images) or 25,000 (2D images) arbitrary units (a.u.). Seed points were then placed near the superior edge of the brain volume and grown to fill the SSS and the surrounding brain tissue (Fig. S1b). Then, the seventh-echo magnitude image (Fig. S1c) was used to segment the rest of the brain volume. The second step enabled the correct exclusion of areas of signal drop-out caused by the presence of air-tissue interfaces (arrows in Fig. S1c). At this stage, the foreground was identified as the part of the image with intensities greater than 150,000 (3D images) or 7,000 a.u. (2D images), seed points were placed across the brain volume and grown to fill the whole brain. The final mask was given by the union of the masks created at the first and second segmentation steps (Fig. S1d).

Finally, to remove morphological noise the whole-brain segmentation was processed using the same sequence of morphological opening and closing operations. Morphological opening applies image erosion followed by image dilation, whereas morphological closing applies image dilation followed by image erosion. Morphological opening and closing were performed using the same 3D spherical

structuring element with a 2-voxel radius. This sequence of morphological operations on the brain mask enabled the removal of small connected components and small protrusions (image opening) and then the filling of small holes and gaps between connected components (image closing).

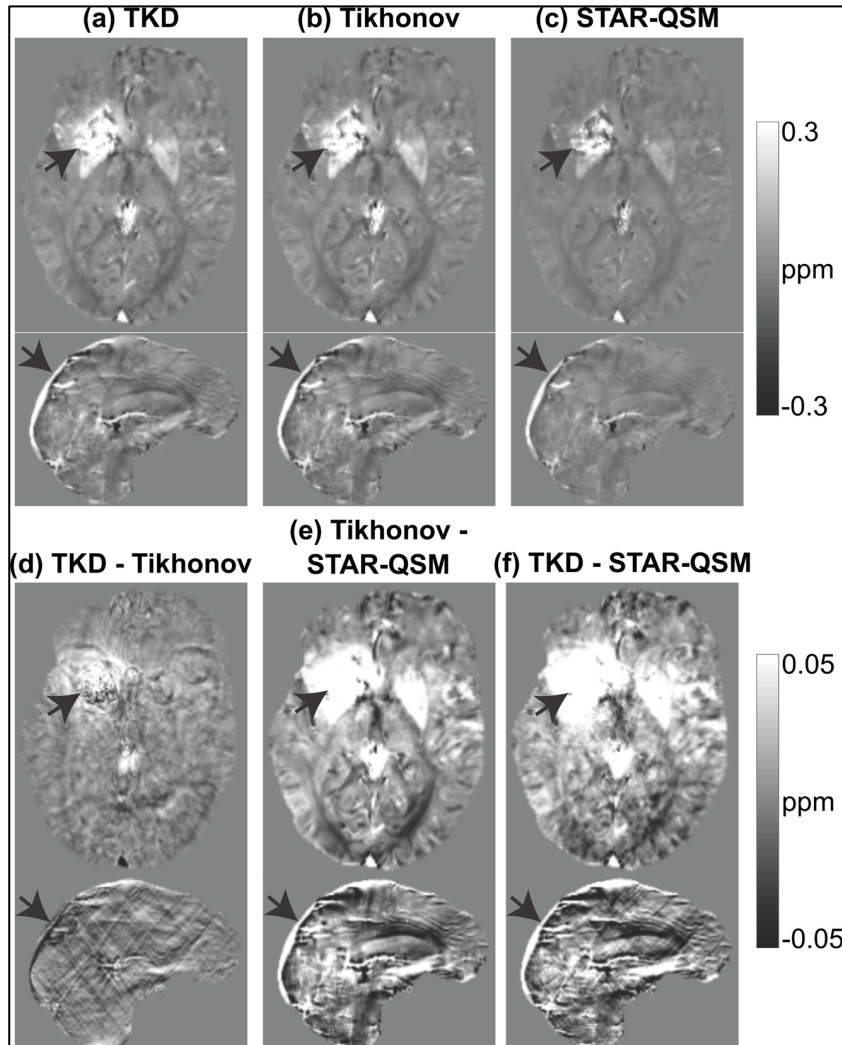


Fig. S2 Comparison of field-to-susceptibility inversion methods. The top row shows the same transverse and sagittal slices of the susceptibility maps calculated using TKD **(a)**, Tikhonov regularization **(b)** and STAR-QSM **(c)**. The bottom row shows the susceptibility difference images for each pair of methods **(d-f)**. In each transverse image, the arrows point at hyper-intense haemosiderin deposits caused by previous bleeding of the AVM. In each sagittal image, the arrows point at the superior sagittal sinus.

S1.2 Choice of a Method for Local Field-to-Susceptibility Inversion

We considered several methods for performing the local field-to-susceptibility inversion step: thresholded k-space division (TKD) (Shmueli et al., 2009), Tikhonov regularization (Kressler et al., 2010) and streaking artifact reduction for quantitative susceptibility mapping (STAR-QSM) (Wei et al., 2015).

By simply truncating the inverse magnetic dipole in k-space, TKD offers the simplest solution to the ill-posed inverse problem. However, because of truncation, QSM images calculated using TKD suffer from streaking artifacts and χ underestimation. This second issue can be addressed by applying a correction based on the point spread function (PSF) of the dipole modification in k-space (Schweser et al., 2013).

Tikhonov-based L_2 regularization aims to minimize the norm of the estimated χ and has the following closed-form solution in k-space:

$$\hat{X}(\mathbf{k}) = B_0 \frac{D(\mathbf{k})}{D^2(\mathbf{k}) + \lambda} \Delta B_{loc}(\mathbf{k}) \quad [S1]$$

where \hat{X} , D and $\Delta B_{loc}(\mathbf{k})$ respectively are the Fourier transforms of the estimated χ , the magnetic dipole and the local field map, λ is the regularization parameter and B_0 the static magnetic field strength. In Eq. S1, the modification of the magnetic dipole induced by regularization in k-space can be isolated from the other terms of the equation. Therefore, it is possible to apply the same PSF-based correction designed for TKD (Schweser et al., 2013) to χ calculated according to Eq. S1. Notably, in the 2016 QSM Reconstruction Challenge (Langkammer et al., 2018), the Tikhonov-regularized solution with such a correction for χ underestimation outperformed STAR-QSM in terms of region of interest (ROI)-based χ accuracy.

STAR-QSM is a two-step method based on L_1 regularization and is designed to reconstruct both small and large χ values. STAR-QSM has been suggested for use in the presence of large susceptibility sources such as those linked to hemosiderin deposits due to a previous hemorrhage.

To evaluate the optimal local-field-to-susceptibility inversion method, TKD, Tikhonov-based regularization and STAR-QSM were tested on the pre-GKR patients. The optimal parameter for Tikhonov-based regularization (λ) was calculated based on the L-curve method (Hansen and O'Leary, 1993) and was equal to 0.0684 (see main manuscript, Section 3.1).

Fig. S2 compares TKD, Tikhonov regularization and STAR-QSM susceptibility maps for a representative pre-GKR patient (i.e., AVM04). This subject was chosen to highlight the performance of these distinct methods in an extreme but common case, when the susceptibility maps show hyper-intensities in areas of previous bleeding. Hemorrhage often occurs in AVM patients due to the rupture of the vessels in the malformation. As a consequence, strongly paramagnetic haemosiderin is deposited in the area of the hematoma and causes blooming artifacts in the χ maps (arrows in the transverse images in Fig. S2).

Streaking artifacts were more prominent TKD than in Tikhonov regularization (Fig. S2d) or STAR-QSM (Fig. S2f) but similar in Tikhonov regularization and STAR-QSM (Fig. S2e). TKD and Tikhonov regularization mainly differed in streaking artifacts but not in tissue contrast (Fig. S2d). STAR-QSM had the best performance in reducing blooming artifacts from the haemosiderin deposit (Fig. S2c), but at the expense of global tissue contrast, which appeared lower compared to all other methods (Figs. S2c, e and f). Based on these results, it was chosen to use Tikhonov regularization was chosen to perform local field-to-susceptibility inversion for all subjects.

Pre-GKR patients	Kernel bandwidth (%)	
	LH	RH
AVM01	1.27	1.29
AVM02	1.13	1.24
AVM03	1.34	1.47
AVM04	1.74	1.59
AVM05	1.99	2.65
AVM06	1.23	1.05
AVM07	1.27	1.34
AVM08	2.14	1.80
AVM09	1.46	1.82
AVM10	1.63	1.54
AVM11	1.72	2.26
AVM12	1.52	1.39
AVM13	2.19	1.77
AVM14	2.35	2.01
AVM15	2.57	2.03
Mean \pm SD	1.70 \pm 0.45	1.68 \pm 0.43

Table S2 Bandwidth of the kernel used for the histogram fit in each pre-GKR patient and both brain hemispheres.

S1.3 SvO₂ Histogram Calculation

For each histogram, the optimal bin size was calculated based on the Freedman-Diaconis rule (Freedman and Diaconis, 1981):

$$Bin\ size = 2 \frac{IQR}{n^{\frac{1}{3}}} \quad [S2]$$

where n is the size of the data set and $IQR = Q_3 - Q_1$ is the interquartile range of the data with Q_1 and Q_2 respectively denoting the first and third quartiles. Calculating the bin size based on IQR is less sensitive to the presence of outliers in the data than calculating it based on the difference between maximum and minimum values in the sample or based on the sample's standard deviation. The number of bins in the histogram was then calculated as:

$$Number\ of\ bins = \frac{\max(SvO_2) - \min(SvO_2)}{bin\ size} \quad [S3]$$

where max and min denote the maximum and minimum values of SvO₂ in the brain hemisphere.

The histogram fitting was performed using the *histfit* Matlab function with the number of bins calculated in the previous equation and the *kernel* option. This option performs nonparametric kernel smoothing, where the kernel is normal and has a width that depends on the input data. The kernel bandwidths for the pre-GKR subjects are shown in Table S2. The *histfit* function then evaluates the density at 100 equally spaced points that cover the range of the input SvO₂ data.

Pre-GKR Patient	Size of ROI _{SSS} [mm ³]	Size of ROI _{DV} [mm ³]	Size of ROI _{HealthyVein2} [mm ³]
AVM01	1489	443	451
AVM02	1949	1321	54
AVM03	1920	813	811
AVM04	2152	259	104
AVM05	1309	414	109
AVM06	994	532	57
AVM07	967	1357	633
AVM08	215	500	494
AVM09	955	348	88
AVM10	365	569	25
AVM11	1466	224	-
AVM12	410	56	159
AVM13	3067	31	467
AVM14	568	536	28
AVM15	934	1435	-
Mean ± SD	1251 ± 780	589 ± 451	268 ± 267

Table S3 Sizes of the vein ROIs in the pre-GKR patients. For each pre-GKR patient, the table shows the size of the SSS, draining vein and additional healthy vein ROIs drawn on the gad-T₁-weighted (healthy veins) and gad-TOF MRA images (draining vein) and then coregistered to the image space of the χ map. The mean and SD of the ROI sizes across patients are also reported.

S1.4 Selection of an Additional Healthy Venous ROI for Calculation of SvO₂

Because of the variable AVM anatomy across pre-GKR patients, three distinct veins were considered to draw the additional healthy vein ROI (ROI_{HealthyVein2}). In two patients (AVM11 and 15), a suitable healthy vein for drawing ROI_{HealthyVein2} could not be identified because the AVM drained into all candidate veins.

In six patients (AVM01, 03, 06, 07, 10 and 13), ROI_{HealthyVein2} was drawn on the straight sinus and its size was set to be as close as possible to the size of ROI_{DV} (after coregistration with the corresponding χ map) to allow SvO₂ measurement with comparable partial volume effects. In six other patients (AVM02, 04, 05, 09, 12 and 14), ROI_{HealthyVein2} was drawn on the internal cerebral vein in the hemisphere without the AVM to avoid contamination with blood leaving the malformation. In these subjects, the straight sinus could not be used because it drained blood from the AVM. Moreover, because the internal cerebral veins are small, the sizes of ROI_{HealthyVein2} and ROI_{DV} could not be matched. In one patient (AVM08), ROI_{HealthyVein2} was drawn on a superficial vein in the hemisphere without the AVM. The size of ROI_{HealthyVein2} is reported in Table S3.

SvO₂ was calculated in ROI_{HealthyVein2} as described in Section 2.9 in the main manuscript. The significance of SvO₂ differences in ROI_{HealthyVein2} compared to ROI_{SSS} and ROI_{DV} was tested using the Wilcoxon rank sum test (significance level = 5%). We tested whether ROI_{HealthyVein2} had an SvO₂ similar to ROI_{SSS} (two-tailed test) and smaller than ROI_{DV} (one-tailed test). We also tested whether the baseline SvO₂ difference was smaller than the SvO₂ difference between ROI_{SSS} and ROI_{DV} (one-tailed test).

To investigate whether the baseline SvO₂ value was different in healthy veins and the SSS, the absolute difference between the average SvO₂ in ROI_{SSS} and ROI_{HealthyVein2} was calculated. We then

tested whether this SvO₂ difference was significantly smaller than the SvO₂ difference between the ROI_{DV} and ROI_{SSS} (one-tailed Wilcoxon rank sum test, significance level = 5%).

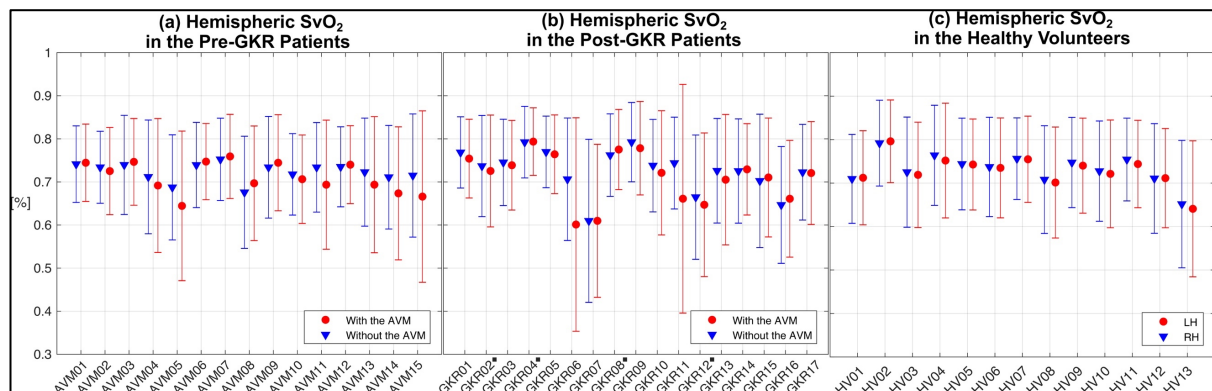


Fig. S3 Hemispheric SvO₂ in the pre-GKR and post-GKR patients and healthy volunteers. The mean SvO₂ values in the pre-GKR (a) and post-GKR patients (b) and healthy volunteers (c) are shown for the brain hemispheres with and without the brain AVM (a, b) and for the left and right hemispheres (c). In (b), the patient tags with a black diamond symbol denote the presence of residual AVM after GKR. The error bars denote the SD of the measurements.

S2. Supplementary Results

S2.1. Hemispheric SvO₂

For the calculation of hemispheric SvO₂, 7 ± 11 and 5 ± 6 voxels were respectively excluded from the left and right hemispheres of all subjects, because they had SvO₂ values outside the 0-100% range. This was always less than 1% of the total number of voxels in the vessel mask in each hemisphere.

Fig. S3 shows the hemispheric SvO₂ means in the pre-GKR (Fig. S2a) post-GKR patients (Fig. S2b) and healthy volunteers (Fig. S2c). In the patients, hemispheric SvO₂ was similar in the hemisphere with the AVM (pre-GKR: $71.16 \pm 3.51\%$; post-GKR: $71.15 \pm 5.76\%$) and without the AVM (pre-GKR: $72.34 \pm 2.09\%$; post-GKR: $72.66 \pm 4.96\%$) both before (pre-GKR) and after radiosurgery (post-GKR). Similar means and SDs of the SvO₂ were also found in the healthy volunteers (left hemisphere: $72.85 \pm 3.60\%$; right hemisphere: $73.29 \pm 3.43\%$).

In the pre-GKR patients, the normal kernel used for the histogram fit of the hemispheric SvO₂ had a bandwidth equal to $1.70 \pm 0.45\%$ in the LH and to $1.68 \pm 0.43\%$ in the RH. Fig. S4 shows the histograms of the SvO₂ in the left and right hemispheres of two pre-GKR patients. The histograms of these subjects are shown because they had the largest inter-hemispheric differences in venous density (Fig. 4a). Therefore, any difference between the SvO₂ values in the AVM's draining veins and the rest of the venous network would be expected to be detected in these subjects.

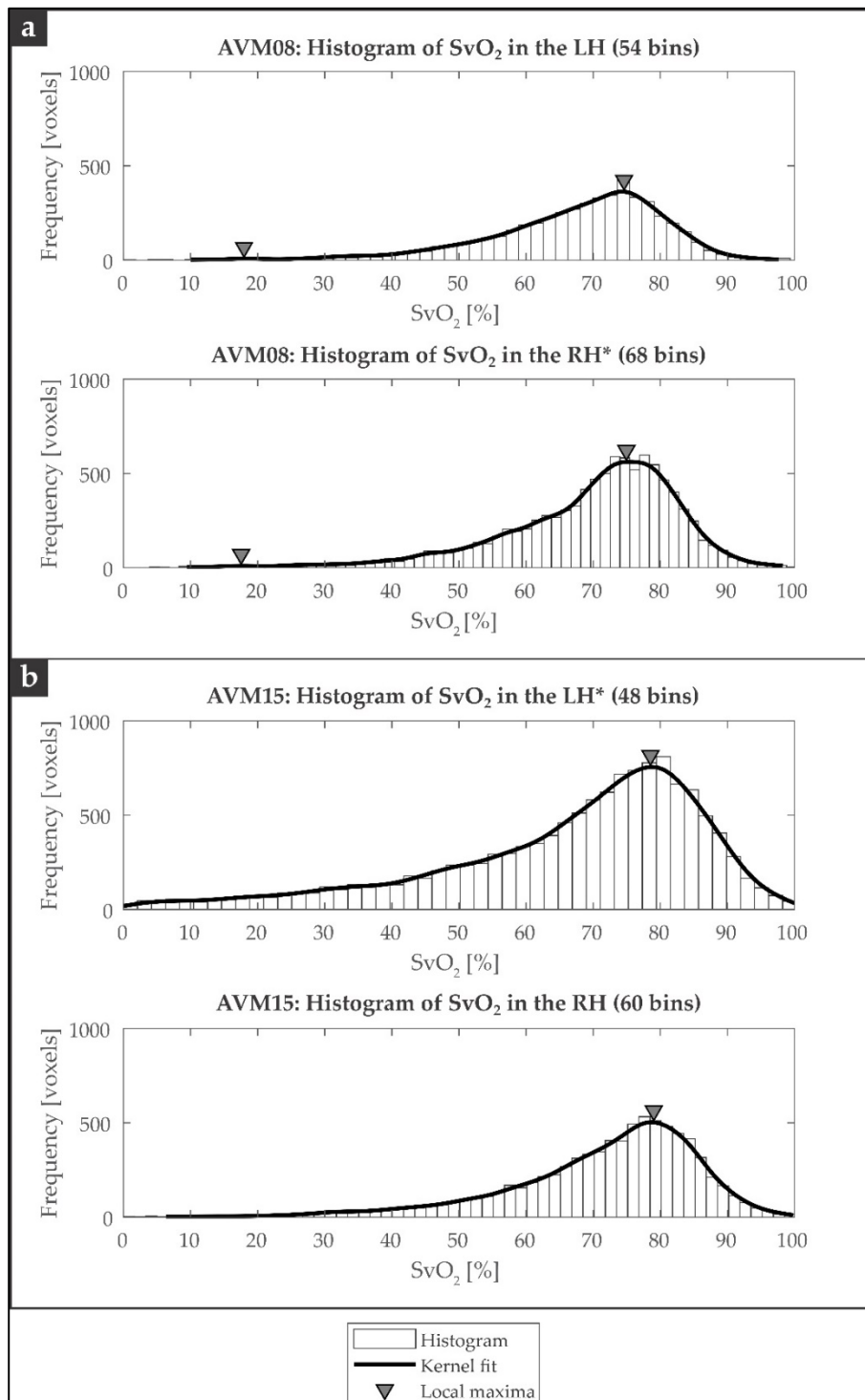


Fig. S4 Histogram of hemispheric SvO₂ in two representative pre-GKR patients, i.e., AVM08 (**a**) and AVM15 (**b**). The solid black line is the result of the histogram fit. The arrowheads point at the local maxima of the fitted line. In the plot titles, the asterisk denotes the hemisphere containing the AVM.

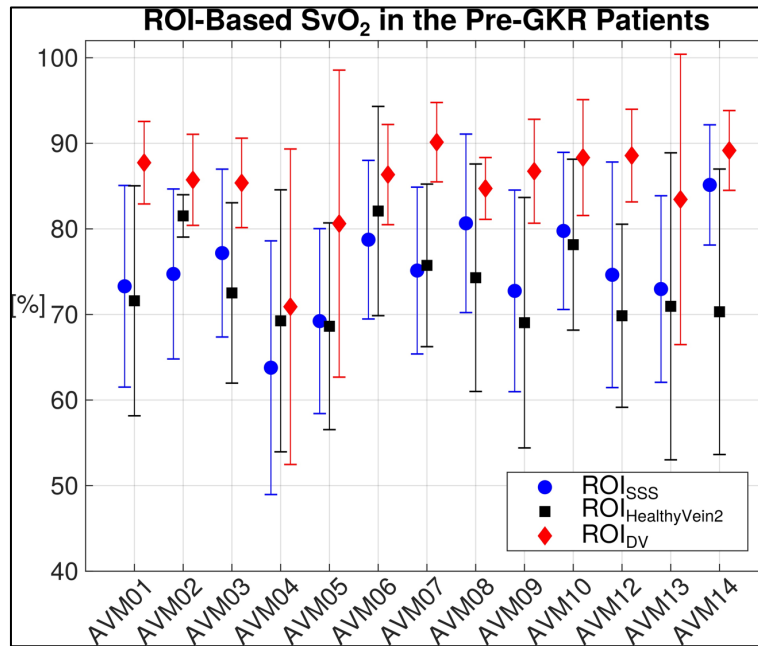


Fig. S5 ROI-based SvO₂ measurements in all three venous ROIs in thirteen pre-GKR patients. In addition to the ROIs shown in Fig. 7 in the main manuscript, the figure shows the mean and SD of SvO₂ measured in a second healthy vein (ROI_{HealthyVein2}). The error bars denote the SD of the measurements.

S2.2 ROI-Based SvO₂

For the calculation of ROI-based SvO₂, 6 ± 9 voxels were removed from ROI_{HealthyVein2} because their corresponding SvO₂ value was outside the 0-100% range. SvO₂ was always larger in ROI_{DV} than in both ROI_{SSS} and ROI_{HealthyVein2}. The means and SEMs of SvO₂ in ROI_{HealthyVein2} across the thirteen pre-GKR patients in Fig. S5 were equal to $75.23 \pm 1.49\%$. SvO₂ was found to be significantly higher in ROI_{DV} than in ROI_{HealthyVein2} ($p < 0.001$) but similar in ROI_{SSS} and ROI_{HealthyVein2} ($p = 0.22$). The difference between SvO₂ in ROI_{DV} and ROI_{SSS} was found to be significantly higher than the absolute difference between SvO₂ in ROI_{SSS} and ROI_{HealthyVein2} ($p < 0.001$). These results provide additional evidence of a significant SvO₂ increase in AVM draining veins compared to healthy veins.

References

- Freedman, D., Diaconis, P., 1981. On the histogram as a density estimator: L2 theory. *Zeitschrift für Wahrscheinlichkeitstheorie und Verwandte Gebiete* 57, 453-476, <http://dx.doi.org/10.1007/bf01025868>.
- Hansen, P.C., O'Leary, D.P., 1993. The Use of the L-Curve in the Regularization of Discrete Ill-Posed Problems. *SIAM Journal on Scientific Computing* 14, 1487-1503, <http://dx.doi.org/10.1137/0914086>.
- Kressler, B., et al., 2010. Nonlinear regularization for per voxel estimation of magnetic susceptibility distributions from MRI field maps. *IEEE Trans Med Imaging* 29, 273-281, <http://dx.doi.org/10.1109/TMI.2009.2023787>.
- Langkammer, C., et al., 2018. Quantitative susceptibility mapping: Report from the 2016 reconstruction challenge. *Magn Reson Med* 79, 1661-1673, <http://dx.doi.org/10.1002/mrm.26830>.
- Schweser, F., et al., 2013. Toward online reconstruction of quantitative susceptibility maps: superfast dipole inversion. *Magn Reson Med* 69, 1582-1594, <http://dx.doi.org/10.1002/mrm.24405>.

Shmueli, K., et al., 2009. Magnetic susceptibility mapping of brain tissue in vivo using MRI phase data. *Magn Reson Med* 62, 1510-1522, <http://dx.doi.org/10.1002/mrm.22135>.

Wei, H., et al., 2015. Streaking artifact reduction for quantitative susceptibility mapping of sources with large dynamic range. *NMR Biomed* 28, 1294-1303, <http://dx.doi.org/10.1002/nbm.3383>.